



Highly stable and robust bi-electrodes interfacial protective films for practical lithium metal batteries

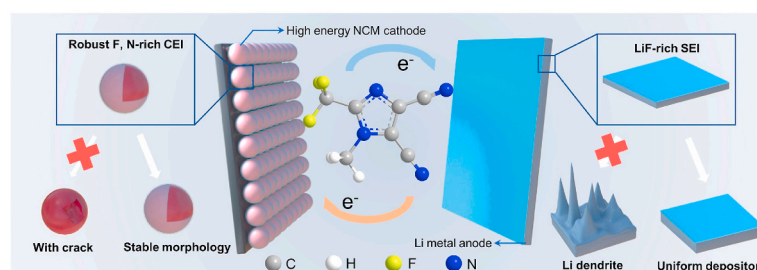
Zhipeng Wen, Hang Li, Huiyang Li, Haiming Hua, Feng Wang, Yu Gu, Yang Yang^{**}, Jinbao Zhao^{*}

State Key Lab of Physical Chemistry of Solid Surfaces, Collaborative Innovation Centre of Chemistry for Energy Materials, State-Province Joint Engineering Laboratory of Power Source Technology for New Energy Vehicle, Engineering Research Center of Electrochemical Technology, Ministry of Education, College of Chemistry and Chemical Engineering, Xiamen University, Xiamen, 361005, Fujian, China

HIGHLIGHTS

- The $C_6F_3LiN_4$ is prior to form films on bi-electrodes more preferentially.
- The lithium dendrites suppression is verified by experiment and simulation.
- Highly stable electrochemical performance in practical Li metal batteries has been achieved.
- This work reveals the importance of bi-electrode film in practical applications.

GRAPHICAL ABSTRACT



ARTICLE INFO

Keywords:

Bi-electrode SEI film
 $C_6F_3LiN_4$
 Li metal anode
 High loading NCM
 Pouch cells

ABSTRACT

Unstable solid electrolyte interphase between lithium metal and electrolyte results in low coulombic efficiency and limited cycle life, which hinder the utility of lithium metal anode. Besides, how to settle the cathode material corrosion in practical lithium metal batteries is also a key challenge. Here, lithium 2 trifluoromethyl-4,5-dicyanoimidazole ($C_6F_3LiN_4$) is reported as valid electrolyte additive for bi-electrode protective films formation in practical Li metal-based batteries. The $C_6F_3LiN_4$ plays distinct functions in bi-electrode interface, it attributes to robust F, N-rich polymer interphase layer on the cathode which effectively protect the cathode from deterioration. And it promotes the even distribution of LiF and polycarbonate species on anode and prevent the formation of Li dendrites. The symmetric cell of $C_6F_3LiN_4$ exhibits stable cycling performance with 1 mA cm^{-2} (700 h). In addition, the improvement in the Li metal deposition uniformity has been confirmed by atomic force microscope and simulation. Benefiting from the synergistic enhanced stability and uniformity of electrode interphase, the $LiNi_{0.5}Co_{0.2}Mn_{0.3}O_2 || Li$ metal battery with $C_6F_3LiN_4$ can maintain high capacity retention of 82.6% after 400 cycles. Importantly, the Li metal pouch battery pairing high-loading cathode (16.12 mg cm^{-2}) also deliver longer cycle life, validating its feasibility in practical applications.

* Corresponding author.

** Corresponding author.

E-mail addresses: yangyang@gdut.edu.cn (Y. Yang), jbzhao@xmu.edu.cn (J. Zhao).

<https://doi.org/10.1016/j.jpowsour.2021.230370>

Received 20 July 2021; Received in revised form 5 August 2021; Accepted 9 August 2021

Available online 14 August 2021

0378-7753/© 2021 Elsevier B.V. All rights reserved.

1. Introduction

Lithium-ion batteries (LIB) are one of most successful commercial rechargeable batteries in the 1990s and are widely used in portable electronic products [1,2]. However, with the rapid development of electric vehicles, aerospace, high-end communication terminals, and large-scale energy storage power stations, the development of high specific energy battery systems with Li metal has become popular in both scientific research and industry [3–7]. Due to the highest specific capacity (3860 mAh g^{-1}) and the lowest redox potential (-3.04 V SHE), lithium is considered to be the ultimate anode material. Coupling sulfur cathode, or oxygen cathode with Li metal to fabricate Li-S [8,9], Li-O₂ [10] batteries can obtain higher theoretical energy density, but the shuttle effect of polysulfide ions and the low catalytic efficiency led to limited cycle life. Among the cathode materials for LIBs that have been discovered, the $\text{LiNi}_{1-x-y}\text{Co}_x\text{Mn}_y\text{O}_2$ (NCM) ($>180 \text{ mAh g}^{-1}$) first reported by JR Dahn exhibits a higher energy density than that of LiCoO_2 (150 mAh g^{-1}) and LiFePO_4 (140 mAh g^{-1}) [11,12]. In addition, its layered structure and tunnel structure are conducive to the deintercalation of Li ions, contributing to the good structure stability. Based on these, the NCM || Li metal-based batteries are considered to be the closest to commercialized energy storage battery system, and corresponding research has also begun to emerge [13,14].

During the initial charging and discharging process of NCM || Li batteries, due to the contact between the highly reactive electrode material and electrolyte, the catalytic decomposition reaction will inevitably occur at the electrode/electrolyte two-phase interface, leading to the formation of passivation films [15–17]. On the NCM cathode side, the original passivation film generated in the traditional LIB electrolyte is ununiform, so it is easily to be destroyed by the volume swell of cathode material during the cycle. The cracks of the passivation film will exacerbate the co-inserting of solvent molecules to damage the structure of the electrode active material, and finally shortens the battery cycle life. Adding additives into electrolytes is a widely used approach to promote uniform passivation films on the cathode [18]. For instance, Ha et al. added 1 wt% LiBOB as additive to the electrolyte to form an interface film, which significantly improved the cycle performance of battery [19]. On the Li metal anode side, competitive chemical reaction and electrochemical reaction of Li ions in this passivation layer, resulting in uneven deposition of Li metal [20]. The growth of Li dendrites and the continuous damage and regeneration of the solid electrolyte interface layer (SEI) cause the problem of capacity degradation. The research based on the interface layer of Li metal is the main method of modification and has achieved remarkable results. It can be found that in Li metal-based battery, the stability of SEI layer on the electrode material surface can determine its cycle life. The battery is a systematic project, and it is far from enough to modify the interface layer on the anode or the cathode solely. It is reasonable to predict that the modification of the interface layers on the bi-electrodes simultaneously will improve the electrochemical performance of the battery synergistically [21,22].

Herein, we report an electrolyte additive that can realize bi-electrode interface layer modification for Li metal-based batteries. Lithium 4,5-dicyano-2-(trifluoromethyl)imidazolide ($\text{C}_6\text{F}_3\text{LiN}_4$) is a newly investigated Li salt [23], which is used as the dehumidizer to remove moisture in the electrolyte and reduce the Al corrosion [24,25]. But to the best of our knowledge, there is few researches on the influence of $\text{C}_6\text{F}_3\text{LiN}_4$ as an additive on electrode materials and whole battery system. The DFT calculation results show that the $\text{C}_6\text{F}_3\text{LiN}_4$ additive can form film on the cathode and anode electrodes simultaneously, and the corresponding experimental results (TEM, SEM) also verify the existence of uniform and dense film on the electrode surfaces. In addition, FT-IR, TOF-SIMS and XPS depth profiles results also show that the film formed by $\text{C}_6\text{F}_3\text{LiN}_4$ on the electrode surface is rich in nitrogen-containing organic molecules and LiF. LiF have strong Li ion conductivity and is good inorganic SEI ingredient. And during the TOF-SIMS analysis process, the decomposition mechanism of $\text{C}_6\text{F}_3\text{LiN}_4$ on the electrode surface can be

obtained. The $\text{C}_6\text{F}_3\text{LiN}_4$ will finally promote the generation of long-chain organic molecules and greatly enhance the flexibility of the film. Benefiting from these advantages, the addition of $\text{C}_6\text{F}_3\text{LiN}_4$ improves the cycle performance of NCM || Li batteries at all. The $\text{LiNi}_{0.5}\text{Co}_{0.2}\text{Mn}_{0.3}\text{O}_2$ (NCM 523) battery with $\text{C}_6\text{F}_3\text{LiN}_4$ can still have a capacity retention rate of 82.6% after 400 cycles. And the Li-Li symmetrical cell with $\text{C}_6\text{F}_3\text{LiN}_4$ can maintain low overpotential for 700 h cycling. Furthermore, the improvement of the uniformity of Li metal deposition by $\text{C}_6\text{F}_3\text{LiN}_4$ has been confirmed by AFM spectrum and COMSOL calculation simulation. Therefore, the high-loading NCM (mass loading of 16.12 mg cm^{-2}) cathode and Li metal pouch battery exhibits higher coulombic efficiency and longer cycle life. The results can provide a broader inspiration for practical Li metal-based batteries with high capacity.

2. Experimental

2.1. Material preparation

The electrolyte used is arranged by 1 M lithium hexafluorophosphorus (LiPF_6) dissolved in ethylene carbonate (EC) and dimethyl carbonate solution (DMC) (1:1 in volume) (named “E-baseline”). The $\text{C}_6\text{F}_3\text{LiN}_4$ was purchased from Alfa Aesar Corporation. The Li foil (thickness: $250 \mu\text{m}$) was purchased from Tianjin Celllithium Corporation, and was kept in glove box before employment. All experimental reagents were used after accepted, and no purification process was performed.

To select the best $\text{C}_6\text{F}_3\text{LiN}_4$ additive concentration, the mass amount of 1%, 2%, 3% and 4% $\text{C}_6\text{F}_3\text{LiN}_4$ was dissolved to the E-baseline electrolyte to prepare (named “E-1% $\text{C}_6\text{F}_3\text{LiN}_4$, E-2% $\text{C}_6\text{F}_3\text{LiN}_4$, E-3% $\text{C}_6\text{F}_3\text{LiN}_4$, E-4% $\text{C}_6\text{F}_3\text{LiN}_4$ ”). In the preparation process, the NCM 523 cathode material, poly(vinylidene fluoride) (PVDF) were mixed in N-methyl pyrrolidone (NMP) and acetylene black are mixed in mass ratio of 8:1:1. And then stirred by magnetic stirrer overnight to ensure uniform dispersion. Then put it evenly coated on the aluminum foil and placed in an oven at $80 \text{ }^\circ\text{C}$ to be dried for use.

2.2. Characterization methods

In order to promote the accuracy of morphology results, the cell assemble and disassemble processes were performed in the glove box with oxygen less than 0.01 ppm and water content less than 0.01 ppm. The obtained Li foil was cleaned with DME several times and naturally dried before characterization. The morphology of the Li metal deposition was completed by field emission scanning electron microscope (SEM, Hitachi 4800). The surface morphology of the cathode is characterized by transmission electron microscope (TEM, F30). The CEI state position of the cathode surface are characterized by X-ray scanning microprobe electron energy spectrometer (XPS, Quantum 2000, Physical Electronics). The Time-of-flight secondary ion mass spectrometry (TOF-SIMS) surface spectra was tested at ion species of Bi^{3++} and ion current of 2 nA for cathode electrodes. The surface roughness test of the Li metal anode was conducted by atomic force microscopy (AFM, SPM 5500, Keysight Technologies) inside an Ar-filled glove box. The Fourier transform infrared (FTIR) spectra were collected using a Nicolet IS5 spectrometer (Thermo Fisher).

2.3. Density functional theory (DFT) calculation

The Highest Occupied Molecular Orbital (HOMO) and Lowest Unoccupied Molecular Orbital (LUMO) energy of EC, DMC, diethyl carbonate (DEC) and $\text{C}_6\text{F}_3\text{LiN}_4$ are calculated with the Gaussian 09 software. We use the B3LYP/6-31G(d, p) basis set to optimize the molecule structures.

2.4. Electrochemical measurement

We choose CR2032 coin cell for full cell test, symmetrical cell test and electrochemical impedance test. During in the full cell performance test, the NCM 523 cathode material was cut into the wafer with radius of 12 mm. Then 100 μl electrolyte was consumed in each battery. The test charging and discharging cut-off voltages were controlled to 4.3 V and 3.0 V, respectively. To measure the coulombic efficiency, copper foil was used as current collector for Li metal, and then assembled with Li foil to form half-cell. It was tested under current of 0.5 mA cm^{-2} and Li deposition capacity of 1.0 mA cm^{-2} . In the symmetrical cell assembly process, the Li foil was used as the working electrode and the counter electrode, and the performance tests were performed with deposition capacity of 1.0 mAh cm^{-2} and deposition current density of 1.0 mA cm^{-2} and 2.0 mA cm^{-2} , respectively.

2.5. Pouch cell assembly

In the assembly process of the pouch battery, the high loading NCM material (16.12 mg cm^{-2}) is selected for cathode material, Li belt is used as anode material, and Celgard 2400 is used as separator and copper net was used as current collector. The copper net was initially cut to length of 85 mm and width of 70 mm, and aligned with the length of 37 mm as the tab. Then pressed the Li belt on the copper mesh and match it with the high loading NCM cathode material with slightly smaller area to assemble the pouch cell. After adding 4 ml electrolyte, the final packaging is carried out with hot press machine at temperature of 180 $^{\circ}\text{C}$.

3. Results and discussion

The $\text{C}_6\text{F}_3\text{LiN}_4$ owns CF_3 group and large amounts of N, so we assume that it can effectively promote LiF and nitrogen-containing organic molecules in the interface layer, thereby improving battery performance (Fig. 1a). We first calculated HOMO and LUMO energy levels of

$\text{C}_6\text{F}_3\text{LiN}_4$ additives and commonly used carbonate solvents (EC, DMC, DEC) (Fig. 1b). In previous studies, the lower value of LUMO energy level will lead to lower resistance toward the reduction of molecule, and the higher value of HOMO energy level will lead to lower resistance toward the oxidation of molecule [26,27]. Therefore, $\text{C}_6\text{F}_3\text{LiN}_4$ is prior to form films on cathode and the anode more preferentially compared to carbonate solvents (EC, DMC, DEC), which caters to our conjecture.

During in the NCM cathode material, although the increase of nickel content will increase the energy density, it will also bring about the instability of the material structure [28,29]. The NCM 523 cathode material has higher energy density and better cycling performance, so it was selected as the electrode material for testing. In the NCM battery cycle under different $\text{C}_6\text{F}_3\text{LiN}_4$ additive mass amounts, the electrochemical performance is best when the mass amount is 1% (Fig. S1). It can be found that the E-1% $\text{C}_6\text{F}_3\text{LiN}_4$ exhibits 160.1 mAh g^{-1} in first cycle (Fig. 2a). Undergoing cycling 400 times, the E-1% $\text{C}_6\text{F}_3\text{LiN}_4$ can still guarantee 132.2 mAh g^{-1} (capacity retention of 82.6%), and maintain relatively stable coulombic efficiency throughout the process. By comparison, the capacity retention rate maintains only 46.8% after 400 cycles with E-baseline electrolyte. In order to compare the voltage curve and different cycling state more intuitively, the capacity retention is chosen as the abscissa. The capacity retention of E-baseline electrolyte decays to below 90% after 100 cycles (Fig. 2b). In the previous reports, the voltage gap when discharge capacity achieves the half of most can report charge/discharge difficulty (Table S1) [30,31]. Therefore, the voltage gap of E-1% $\text{C}_6\text{F}_3\text{LiN}_4$ cell remained at low level (38 mV) after 100 cycles, and the overpotential only increased to 136 mV even after 400 cycles. In contrast, the voltage gap of E-baseline cell in the initial state has reached 153 mV, and, the voltage gap continues to increase (Fig. 2c). The increase means that the interface is hindering the insertion of Li ions, resulting in the decline in discharge capacity.

In order to further explore the reason for its capacity decay, the electrochemical impedance test has been carried out in (Fig. 2d). The impedance under the E-baseline increases quickly with the deepening of

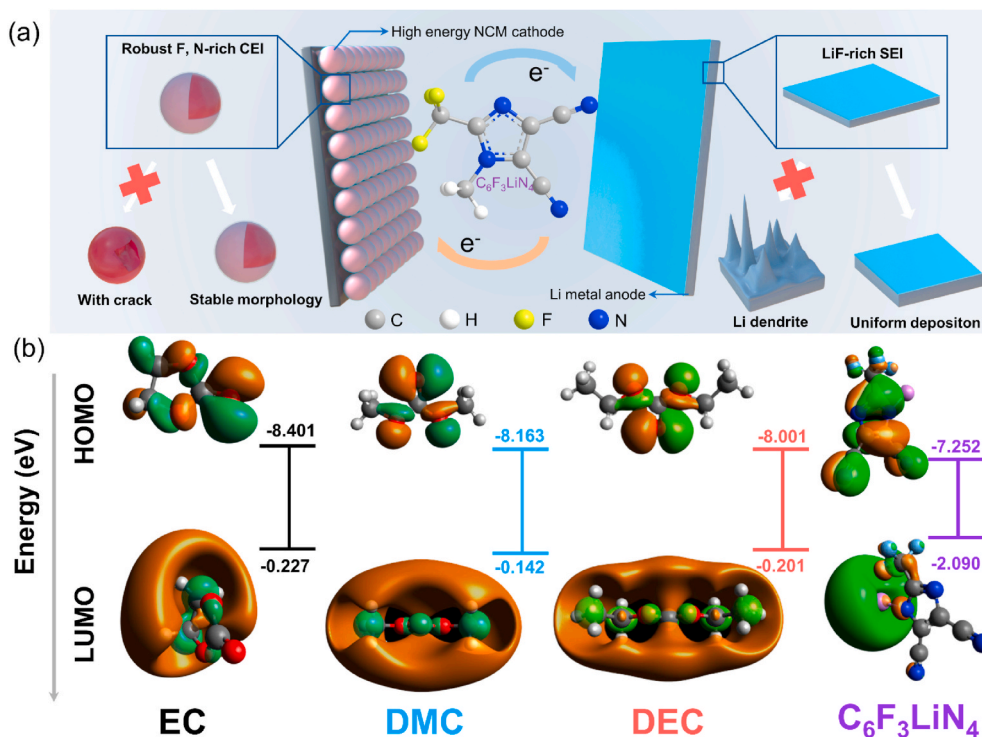


Fig. 1. Schematic of the dual-function of $\text{C}_6\text{F}_3\text{LiN}_4$ additive in Li metal-based batteries bi-electrode. (a). Schematic figure of the electrode composition of Li metal-based batteries with $\text{C}_6\text{F}_3\text{LiN}_4$ additive. (b). Calculated values of the HOMO and LUMO energy levels of different carbonated solvent (EC, DMC, DEC) and $\text{C}_6\text{F}_3\text{LiN}_4$ additive.

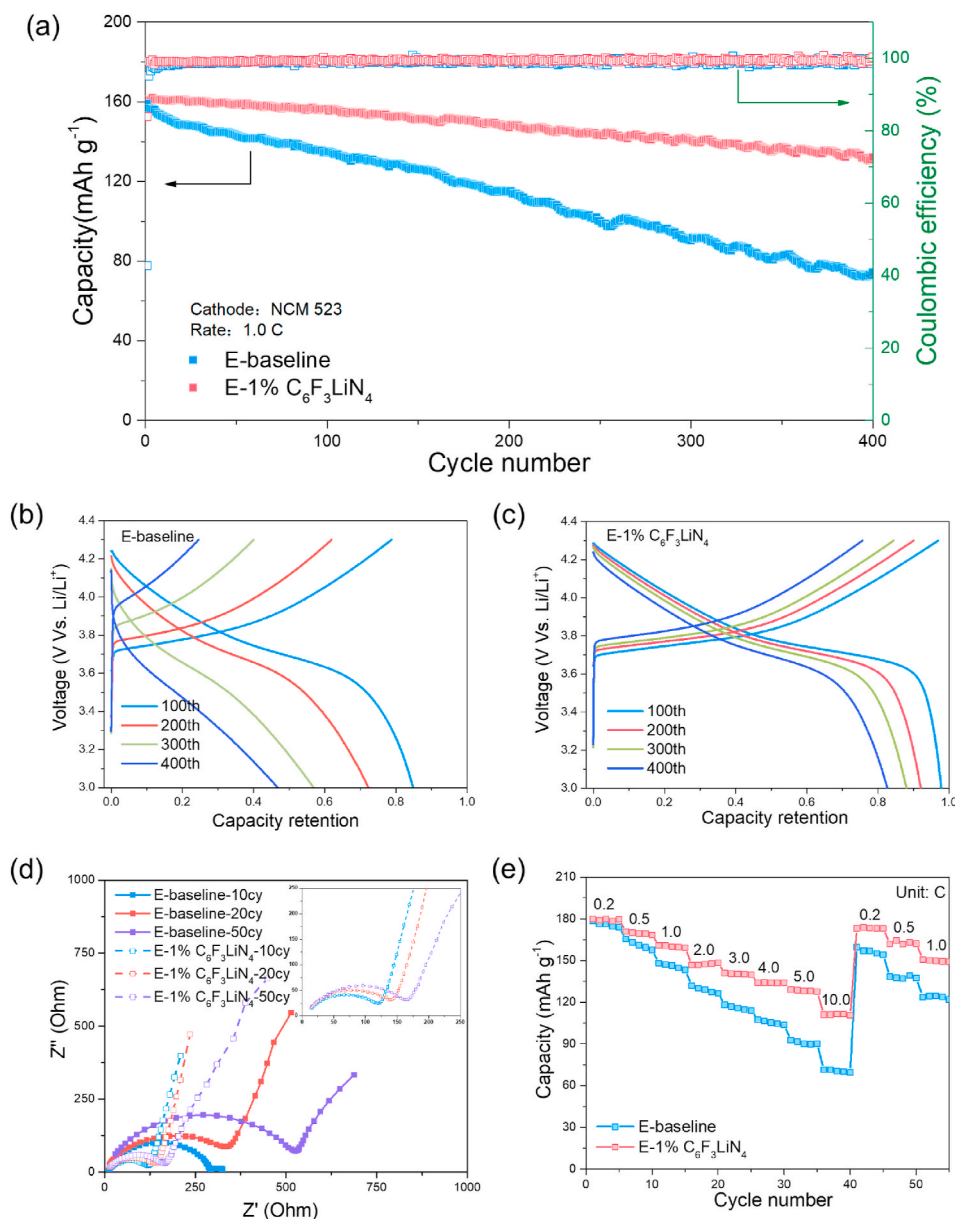


Fig. 2. Electrochemical performance of NCM 523/Li metal batteries using different electrolyte. (a) Cycling performance with NCM 523 cathode (mass loading of 5 mg cm^{-2}) at the current density of 1.0 C (corresponding to 0.90 mA cm^{-2}). The voltage-capacity retention curves of NCM 523/Li metal batteries with E-baseline electrolyte (b) and E-1% $\text{C}_6\text{F}_3\text{LiN}_4$ electrolyte (c). (d) The electrochemical impedance spectra of NCM 523/Li metal batteries after 10, 20 and 50 cycles using different electrolyte. (e) Rate capacity test of NCM 523/Li metal batteries.

the cycle, indicating that the instability of the interface causes the thickening of the interface layer. For comparison, the impedance with E-1% $\text{C}_6\text{F}_3\text{LiN}_4$ is significantly lower than E-baseline after 10 cycles (Fig. S2), which proves that the promoted CEI is more conducive to the insertion of Li ions. And after 20, 50 cycles, the mass transfer impedance (R_{ct}) basically does not change too much, which demonstrates that the protective layer promoted by E-1% $\text{C}_6\text{F}_3\text{LiN}_4$ has good stability (Table S2). During in the rate cycle performance test, the E-1% $\text{C}_6\text{F}_3\text{LiN}_4$ cell shows more obvious advantages especially under 5C and 10C, it can still release 128.5 mAh g^{-1} and 110.1 mAh g^{-1} . In contrast, the E-baseline cell can only release 91.5 mAh g^{-1} and 71.3 mAh g^{-1} . During the entire electrochemical cycle, the solid-phase mass transfer is slowest, which is the rate-determining step. Therefore, the higher discharge capacity at high rate means that the interface of the E-1% $\text{C}_6\text{F}_3\text{LiN}_4$ electrode surface is more beneficial to the insertion and extraction of Li ions (Fig. 2e).

On the cathode side, the surface of cathode particles will spontaneously form a coating layer of cathode electrolyte interface. The protective layer can effectively reduce the parasitic reaction, and prevent the dissolution of metal ions. In order to check the state of CEI, the NCM 523

particles were tested by TEM (Fig. S3). The N, O and F elements are well distributed on the NCM 523 cathode particle surface. And through the image where all the elements overlap, it can be known that the generated CEI is distributed very smoothly. To further understand the position relationship between the CEI and the cathode material particle, the NCM 523 cathode material after cycling has been cut with three ion beams, and finally got the interface SEM image of single NCM 523 cathode particle, as shown in (Fig. 3a). After overlapping the distribution maps of Ni, C and F elements, the C and F elements are basically on the surface of the particles. In element mapping images, the Ni element represents NCM 523 particle, while C and F represent the CEI formed on the surface. As shown in Fig. 3b, the coating under the E-baseline shows uneven distribution, which could not effectively protect the cathode material during long cycles. Therefore, the NCM 523 cathode particles appeared microcracks due to the volume change caused by the detachment after 50 cycles (Fig. 3c). After 200 cycles, the uneven interface layer generated under the E-baseline cannot effectively protect the cathode material from further crushing, and the entire particle has been destroyed (Fig. 3d). In Fig. 3e, uniform protective layer (7 nm) can be seen under the E-1% $\text{C}_6\text{F}_3\text{LiN}_4$ electrolyte. Benefiting from the uniform and stable

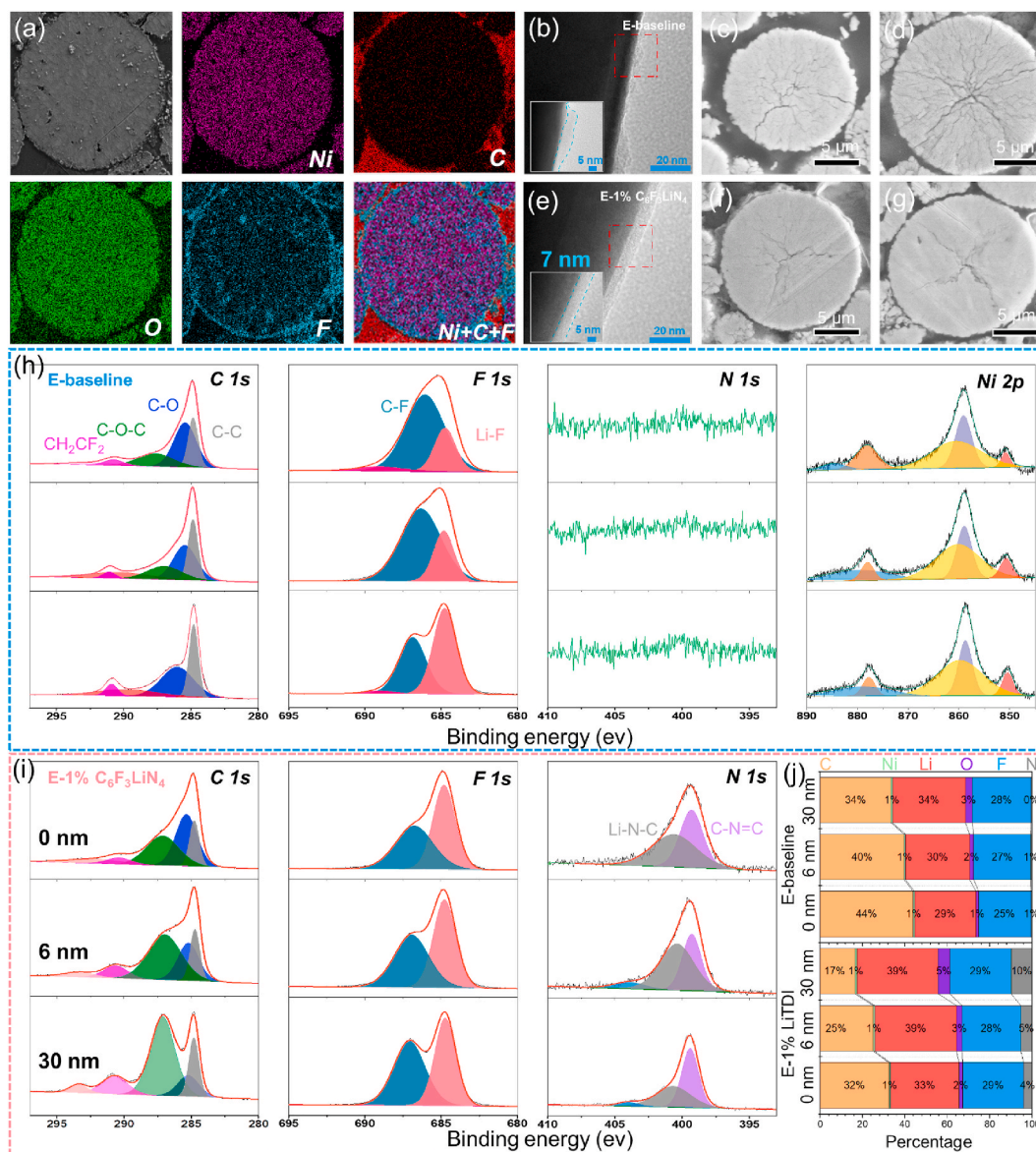


Fig. 3. Morphology and chemistry of CEI with E-1% $C_6F_3LiN_4$ electrolyte. (a). Cross-sectional SEM image and the corresponding element mapping images of NCM 523 cathode particles with E-1% $C_6F_3LiN_4$ electrolyte at 1.0 C for 50 cycles. High resolution transmission microscope of NCM 523 cathode surface with E-baseline electrolyte (b) and E-1% $C_6F_3LiN_4$ electrolyte (e). Cross-sectional SEM images of NCM 523 cathode particles after 50 (c) and 200 (d) cycles in E-baseline electrolyte. Cross-sectional SEM images of NCM 523 cathode particles after 50 (f) and 200 (g) cycles in E-1% $C_6F_3LiN_4$ electrolyte. High resolution XPS spectra at different sputtering depth for different elements of NCM 523 cathode surface cycled in E-baseline electrolyte (h) and E-1% $C_6F_3LiN_4$ electrolyte (i). (j). The proportion of different elements at different depths in CEI.

protective layer, the NCM 523 cathode electrode particles at E-1% $C_6F_3LiN_4$ can maintain stable structure even under long cycles without signs of breakage (Fig. 3f and g).

To better understand the mechanism in improving the stability of the cathode, the XPS depth profiles has carried out to study the properties of the coating protective layer. XPS depth profiles analysis is to explore the interface properties in the longitudinal direction by continuously etching with argon ions (Fig. 3h and i). Since the previous STEM result indicates that the coating protective layer under E-1% $C_6F_3LiN_4$ electrolyte is about 7 nm, so the different sputtering depths of 0, 6, 30 nm is selected. It can be clearly seen in the C 1s spectrum that the C-C (284.8 eV) composition of the coating layer under E-1% $C_6F_3LiN_4$ Greatly reduced, this part mainly comes from the conductive carbon, and the oxidation products of electrolyte [32,33]. In the F 1s spectrum, the Li-F (648.7 eV) on the surface of the E-baseline is less than E-1% $C_6F_3LiN_4$, and the Li-F is considered a good CEI component [34]. During the N 1s

spectrum, it is obvious that the CEI in the E-baseline basically cannot detect a valid signal. In E-1% $C_6F_3LiN_4$ electrolyte, the characteristic peaks of Li-N-C (401.2 eV) and C-N=C (399.3 eV) are clearly distinguished. As the increase of sputtering time, the signal of C-N=C increases, and the signal of Li-N-C reduces, in contrary. In fact, the two signals correspond to different oxidation products of $C_6F_3LiN_4$. In the inner layer of CEI, the $C_6F_3LiN_4$ thoroughly oxidation products (C-N=C) are distributed due to the easier access to electrons. However, because of the low conductivity of CEI, the initial oxidation products of $C_6F_3LiN_4$ (Li-N-C) are distributed in the outer layer of CEI [35,36]. Finally, the content distribution results of different elements at different depths in CEI can be analyzed (Fig. 3j). The contents of Li and F of E-1% $C_6F_3LiN_4$ are significantly higher than those of E-baseline, which shows again that E-1% $C_6F_3LiN_4$ can promote the large-scale production of LiF in CEI. And the F content is basically unchanged from different depths, indicating that the CEI formed by E-1% $C_6F_3LiN_4$ is uniform in thickness

and stable in composition. From the fact that the content of Ni remains basically unchanged, it can also be proved that E-1% $C_6F_3LiN_4$ has no effect on the cathode composition. Therefore, the decomposition of lithium salts and solvents is greatly reduced.

In order to clarify how $C_6F_3LiN_4$ reacts on the NCM 523 cathode material, TOF-SIMS is employed to probe the CEI composition of NCM 523 cathode material. In the beginning, the strong signals of Li^+ and F^- can be detected, which means that the CEI formed under E-1% $C_6F_3LiN_4$ is dominated by LiF (Fig. 4a–c) [37,38]. From the intensity of the characteristic peaks (Li_2F^+ , $Li_3F_2^+$, $Li_5F_4^+$) that E-1% $C_6F_3LiN_4$ will promote the formation of LiF in CEI, that perhaps prevent lattice oxygen exposure. And from results of organic polymers alkane structure, such as $C_2H_3^+$, $C_3H_5^+$, $C_4H_{10}^+$, the CEI under E-baseline is mainly composed of short organic molecular fragments (Fig. 4b), while E-1% $C_6F_3LiN_4$ can greatly promote the formation of long organic molecular fragments (Fig. 4d). Therefore, E-1% $C_6F_3LiN_4$ will greatly improve the flexibility of CEI, corresponding to the capacity retention rate under long cycles.

To better determine the different effects of E-baseline and E-1% $C_6F_3LiN_4$ on the NCM 523 cathode material, the distribution of different molecular fragments (Li_2F^+ , CN^- , Li_3O^+ , $C_{15}H_5^-$) is shown in Fig. 4e and f. Firstly, the E-1% $C_6F_3LiN_4$ electrolyte can promote the distribution of higher density LiF in CEI compared with E-baseline from the Li_2F^+

mapping images, which is consistent with the XPS analysis results. In addition, the CEI under the E-1% $C_6F_3LiN_4$ has larger number of CN^- molecular fragments than E-baseline electrolyte, which means that $C_6F_3LiN_4$ will produce amounts of CN^- during the decomposition process. Benefit from protective layer, it can greatly reduce the generation of Li_2O , which can be verified in the Li_3O^+ mapping images. Finally, long-chain organic molecules are more flexible and denser than short-chain organic molecules, so they are more suitable as a protective layer for cathode materials. Obviously, the CEI generated by E-1% $C_6F_3LiN_4$ also has dominant $C_{15}H_5^-$ molecular fragments, indicating that $C_6F_3LiN_4$ can promote the formation of long-chain organic molecular fragments during its decomposition process [39].

Therefore, combining the TOF-SIMS analysis results and the calculation of bond level change when the $C_6F_3LiN_4$ gains or loses electron (Fig. S4), we assumed the decomposition mechanism of $C_6F_3LiN_4$ on the surface of the NCM 523 cathode (Fig. 4g). Combined with calculation results, after $C_6F_3LiN_4$ gains electrons, the chemical bond of the imidazole ring is weakened, where the chemical bond is most likely to be broken. Therefore, the $C_6F_3LiN_4$ is easy to get electrons and is oxidized to form CN^- molecular fragment (which is verified in the CN^- mapping in Fig. 4f). Finally, $C_6F_3LiN_4$ occurs rearrangement after obtaining oxygen, forming long-chain fused ring polymer with pyrrole, pyridine, and

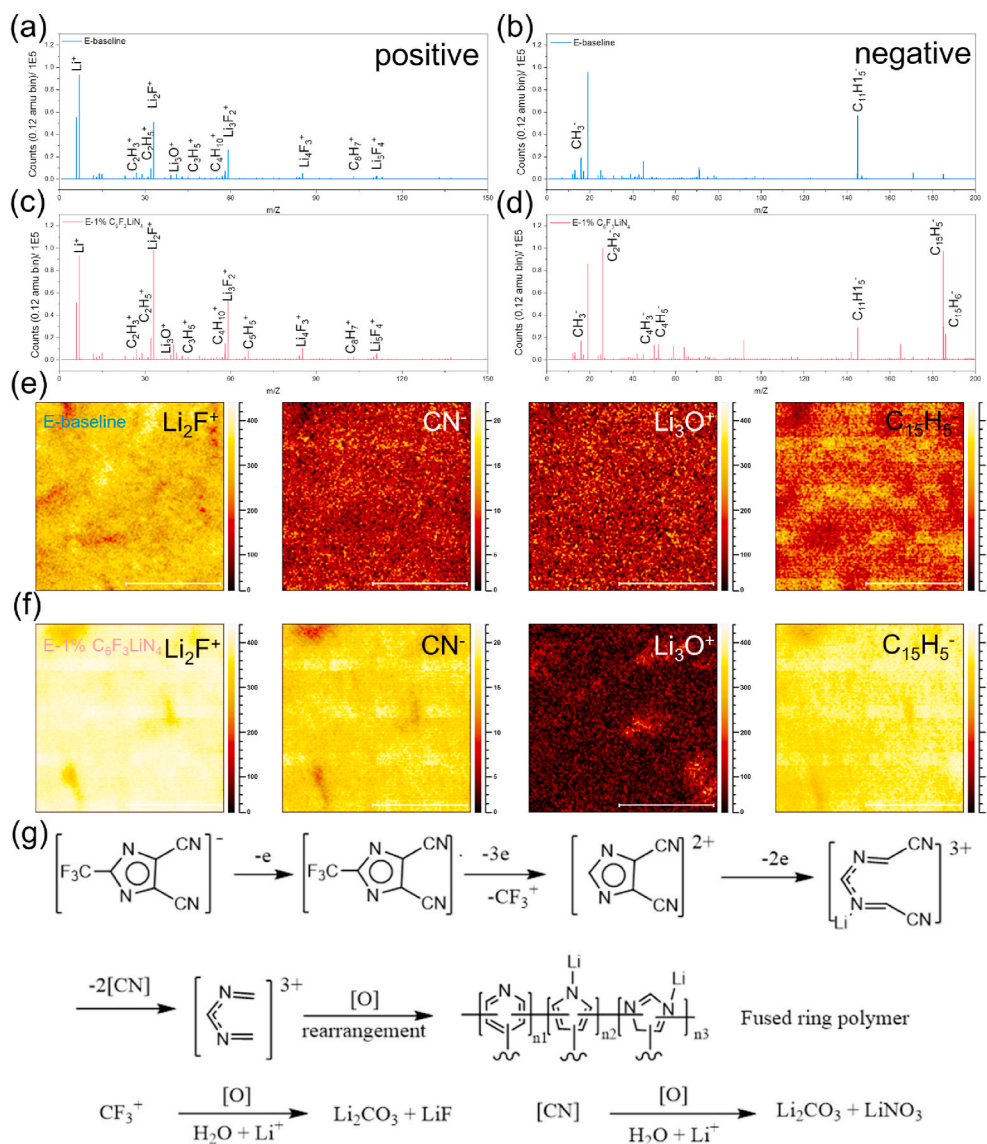


Fig. 4. Reaction mechanism of $C_6F_3LiN_4$ additive on NCM 523 cathode material. TOF-SIMS spectra (positive secondary ion mode and negative secondary ion mode) for NCM 523 cathode electrodes of the E-baseline (a, b) and E-1% $C_6F_3LiN_4$ (c, d) cells cycled at 1.0 C after the 20th cycle. TOF-SIMS analysis of Li_2F^+ , CN^- , Li_3O^+ and $C_{15}H_5^-$ molecular fragment on NCM 523 cathode in E-baseline (e) and E-1% $C_6F_3LiN_4$ (f) electrolyte. (g). The schematic reaction process of $C_6F_3LiN_4$ additive on the NCM 523 cathode material.

imidazole rings. A large amount of CF_3^+ and $[\text{CN}]$ groups are produced during the whole reaction process, which will continue to react with trace water in the electrolyte [CF_3^+ reacts to form Li_2CO_3 and LiF , $[\text{CN}]$ reacts to form Li_2CO_3 and LiNO_3], achieving the purpose of removing water from the battery [40]. In addition, the final reaction product of $\text{C}_6\text{F}_3\text{LiN}_4$ contains many nitrogen-containing molecular products, in which the $\text{C}=\text{N}=\text{C}$ group is verified in the XPS results (Fig. 3i). The LiF can be used as good electrical insulator, which can effectively reduce the contact of NCM 523 cathode material with electrolyte and perhaps prevent lattice oxygen exposure. In all, CEI with flexibility and high Li ion conductivity mixed with organic and inorganic materials can be formed, corresponding to the performance improvement in previous results.

As Li metal-based battery, it is far from enough to improve the property of the NCM 523 cathode material. The interface adjustment on the Li metal side also has a great impact on its electrochemical performance. To explore impact of $\text{C}_6\text{F}_3\text{LiN}_4$ on Li metal side, the Li–Li symmetrical cell and Li–Cu half-cell were used to investigate the performance with E-baseline and E-1% $\text{C}_6\text{F}_3\text{LiN}_4$ electrolyte. The Li–Li symmetrical cell cycling performance under different $\text{C}_6\text{F}_3\text{LiN}_4$ additive mass amounts also proves the best mass amount is 1% (Fig. S5). As shown in Fig. 5a, the E-1% $\text{C}_6\text{F}_3\text{LiN}_4$ can maintain low deposition

overpotential and hold stable cycle for 700 h. For comparison, the overpotential of the E-baseline begins to increase continuously after cycling for 200 h, and occurs the short circuit only after 300 h. It shows that the interface of Li metal under E-baseline is very unstable. After long cycling, dead Li begins to accumulate, resulting in continuous increase in the deposition overpotential. The increase of deposition overpotential aggravates the unevenness of Li metal deposition, promoting the growth of Li dendrites. And finally pierces the separator and causes the short-circuit. The enlarged voltage curve of the cell cycled for 30 h, 230 h, 430 h shows that the E-1% $\text{C}_6\text{F}_3\text{LiN}_4$ exhibits lower deposition overpotential than E-baseline under different cycle times. And its voltage curve also presents typical ‘wedge’ shape. As explored in related reports, the mass transfer effect caused by the accumulation of dead Li will change the shape of the voltage curve of symmetric cell from ‘peak’ to ‘arc’, which is consistent with the trend exhibited by the E-baseline [41,42]. As current increases in 2 mA cm^{-2} , E-1% $\text{C}_6\text{F}_3\text{LiN}_4$ can still maintain low deposition overpotential and stable cycle for 250 h, while E-baseline occurs short circuit after cycling for 200 h (Fig. 5b). To further verify the improvement of $\text{C}_6\text{F}_3\text{LiN}_4$, the Li–Cu half-cell can intuitively see the loss of Li metal during each cycle, so it focuses more on reflecting the barrier effect of the constructed interface on Li metal and electrolyte. As shown in Fig. 5c, the E-baseline can maintain stable

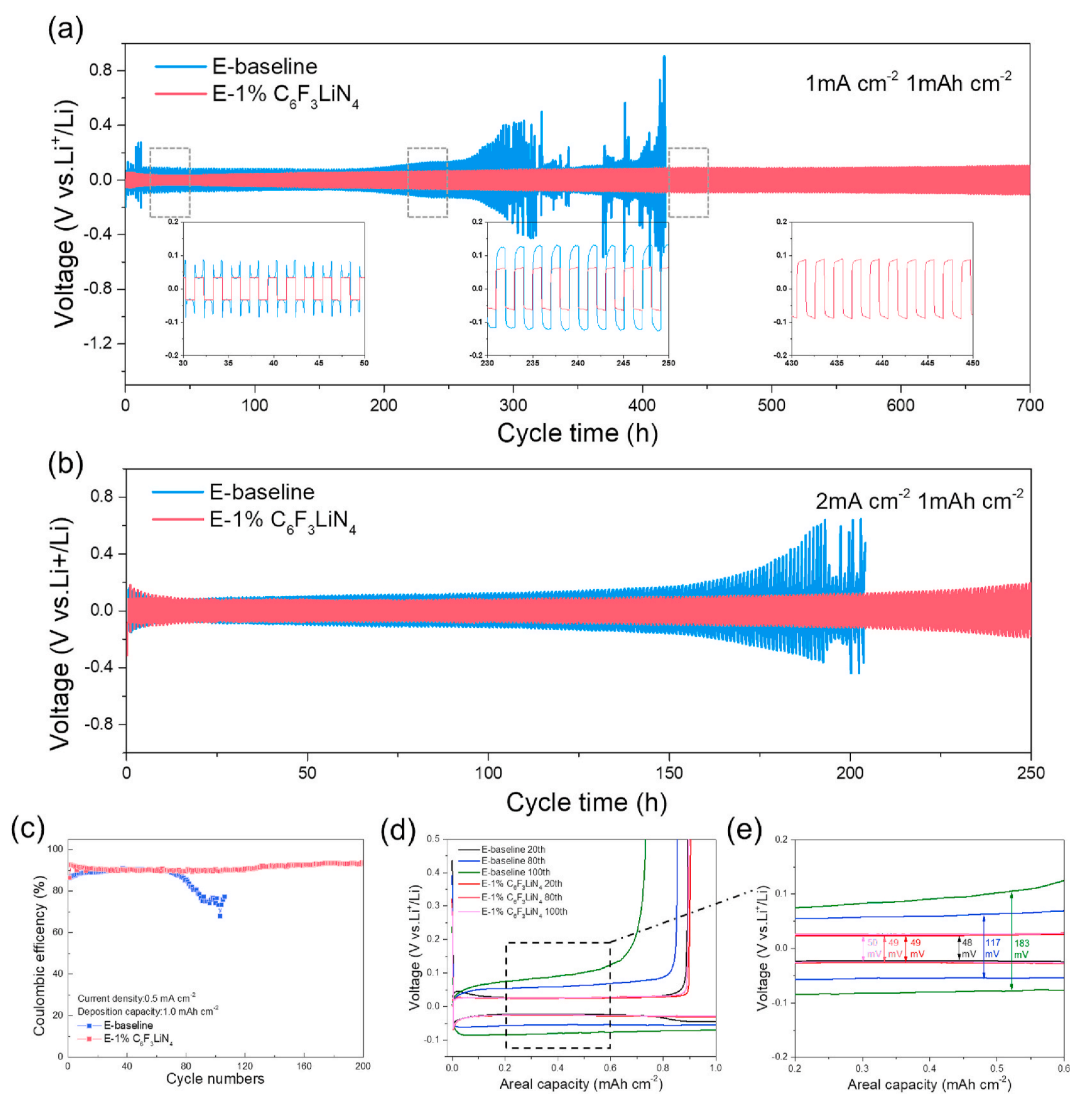


Fig. 5. Comparison of Li metal-based cell electrochemical performance. (a) The symmetric cell performance with 1 mA cm^{-2} and 1 mAh cm^{-2} and selected enlarged voltage profiles. (b) The symmetric cell performance with 2 mA cm^{-2} . (c) The Li–Cu half-cell cycling property with 0.5 mA cm^{-2} and 1 mAh cm^{-2} . The voltage profile of Li–Cu half-cell of different cycles (20th, 80th, 100th) and enlarged voltage profiles.

Li deposition and stripping process during the initial 60 cycles, and the coulombic efficiency begins to drop sharply after 80 cycles of cycling, which indicates that the SEI is extremely unstable. In other words, it needs to consume lots of Li metal to rebuild CEI during each cycle. For comparison, E-1% $C_6F_3LiN_4$ can maintain stable for 200 cycles, and the

coulombic efficiency gradually stabilizes at 93% after 100 cycles. When focusing the capacity-voltage curves at cycle 20th, 80th and 100th, E-1% $C_6F_3LiN_4$ can keep low and stable deposition potential during long cycle (Fig. 5d). However, while the deposition potential of E-baseline increases along with cycling owing to the accumulation of dead, which is

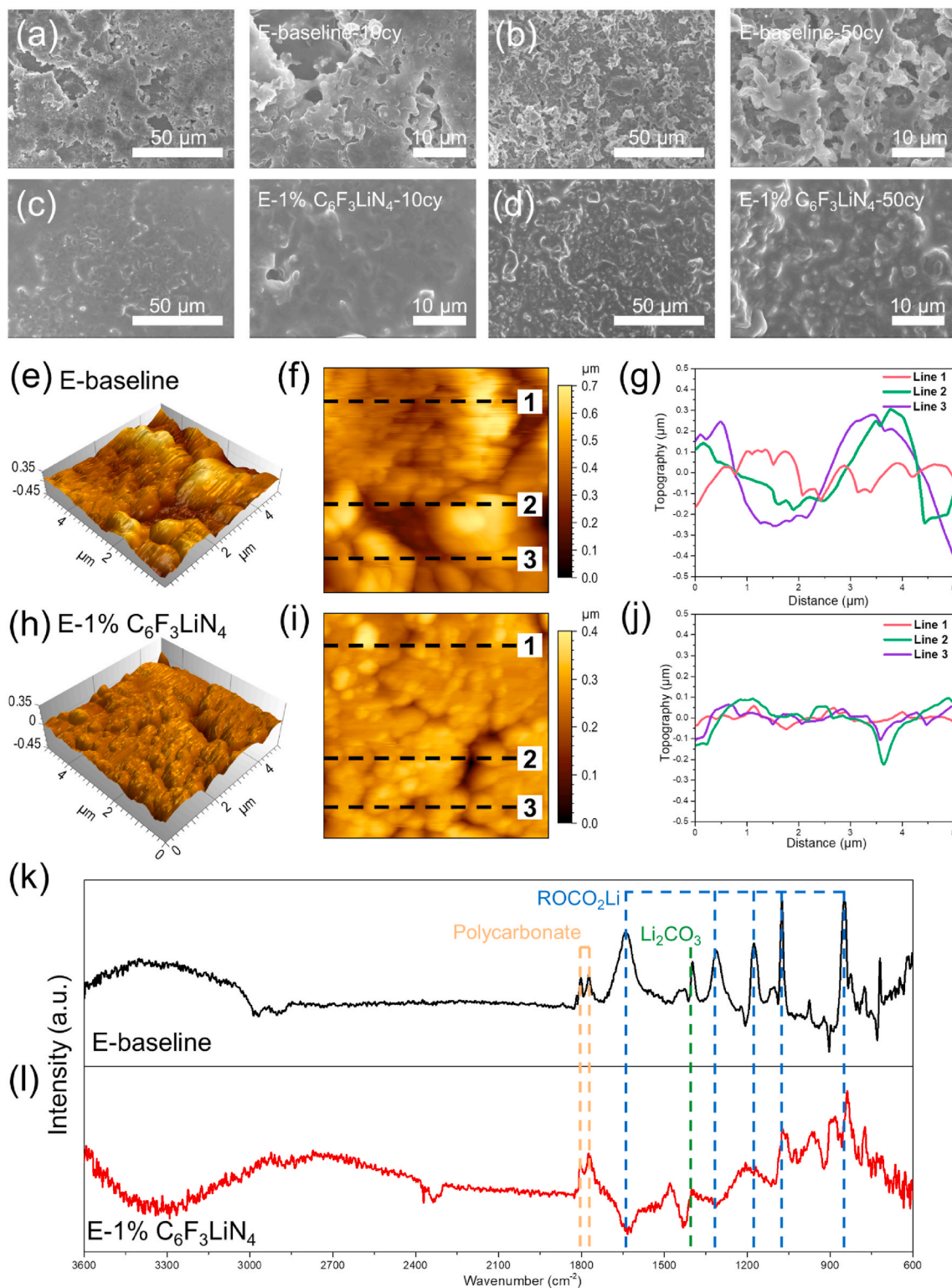


Fig. 6. The Li metal deposition morphology and component analysis. The SEM images of Li metal after 10 cycles (a) and 50 cycles (b) with E-baseline electrolyte and $C_6F_3LiN_4$ electrolyte (c, d). The 3D height AFM images ($5 \mu m \times 5 \mu m$) after 10 cycles with E-baseline (e, f) and E-1% $C_6F_3LiN_4$ electrolyte (h, i). The topography-distance curves along the line 1–3 in AFM images with E-baseline (g) and E-1% $C_6F_3LiN_4$ electrolyte (j). Comparison of FTIR spectra of SEI films after 20 cycles in E-baseline (k) and E-1% $C_6F_3LiN_4$ electrolyte (l).

the same phenomenon as reflected in symmetrical cell (Fig. 5e). In general, $C_6F_3LiN_4$ can not only build a protective layer on the NCM 523 cathode, but also promote the construction of stable SEI layer on anode. As result, addition of $C_6F_3LiN_4$ can ensure that the Li metal cell maintains longer cycle life while also having and higher cycle efficiency.

From the electrochemical performance difference between E-baseline and E-1% $C_6F_3LiN_4$ electrolyte, it can be supposed that E-1% $C_6F_3LiN_4$ can promote more uniform deposition of Li metal, reducing SEI film fragmentation and improving cycle stability. In order to prove the assumption, the SEM images cycled 50 and 100 cycles were carried out in (Fig. 6a–d). The surface of Li metal of E-baseline exhibits uneven and porous morphology after 10 cycles, and with serious cracks (Fig. 6a). The uneven Li metal surface attributes to strong electric field at its tip, which tends to attract more Li ions, leading to the continuous growth of Li dendrites. After 50 cycles, a lot of dead Li generated by the fracture of Li dendrites are distributed on the surface (Fig. 6b). Extensive Li dendrites with needle-like structure can be clearly found, as a result of the instability of SEI film formed under E-baseline electrolyte. In contrast, the morphology of Li metal at E-1% $C_6F_3LiN_4$ exhibits smooth tendency after 10 cycles (Fig. 6c), and no obvious cracks are found even after 50 cycles (Fig. 6d), which proves that E-1% $C_6F_3LiN_4$ can promote the smooth Li metal deposition. To further observe the deposition

morphology, AFM images were used to test the flatness of Li metal (Fig. 6e–j). From the 3D height AFM images, the surface of Li metal at E-1% $C_6F_3LiN_4$ is much flatter than that of E-baseline. It can be seen from the depth curve in line 1–3 that the surface of Li metal under E-baseline is rugged, which intensifies Li dendrites [43]. Finally, to explore reason why Li metal can be deposited smoothly under E-1% $C_6F_3LiN_4$, the FTIR spectroscopy was used to analyze composition of SEI film after 20 cycles. There are two small characteristic peaks (1801 cm^{-1} , 1770 cm^{-1}) belonging to polycarbonate species ($ROCO_2R$) in E-baseline [44,45]. In addition, the characteristic peaks at 1640 cm^{-1} , 1309 cm^{-1} , 1174 cm^{-1} , 1075 cm^{-1} and 850 cm^{-1} of E-baseline electrolyte are stronger than those in E-1% $C_6F_3LiN_4$ electrolyte, which are classified to $ROCO_2Li$ (Fig. 6k). The characteristic peaks distributed around 1300 cm^{-1} are attributed to Li_2CO_3 . In the FTIR spectrum of E-1% $C_6F_3LiN_4$, the polycarbonate species, $ROCO_2Li$ and Li_2CO_3 species can be clearly observed (Fig. 6l). In addition, the polycarbonate species of E-1% $C_6F_3LiN_4$ are richer than E-baseline. Moreover, it has been confirmed in previous work that the $ROCO_2R$ in SEI has stronger viscosity and flexibility than $ROCO_2Li$. Therefore, the Li metal surface constructed by E-1% $C_6F_3LiN_4$ with more polycarbonate species can alleviate the volume expansion in Li metal deposition and stripping process [46]. As a result, it can greatly reduce the fragmentation of SEI, and thus form uniform Li metal

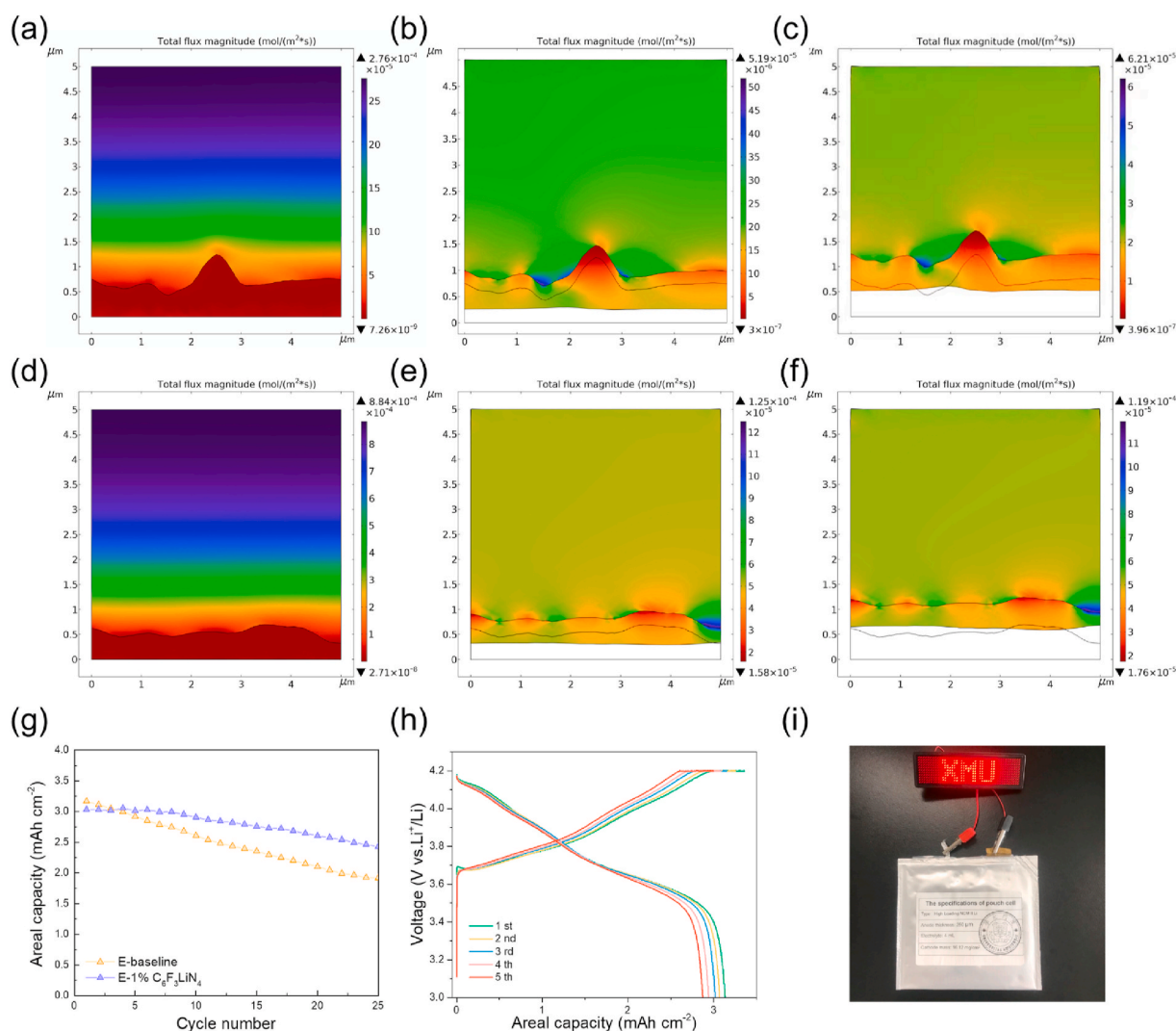


Fig. 7. COMSOL simulations of the Li metal anode in cross-sectional view during E-baseline electrolyte in the pristine state (a), after 2500s (b) and 5000s (c) Li metal deposition in 0.5 mA cm^{-2} . COMSOL simulations with E-1% $C_6F_3LiN_4$ electrolyte in the pristine state (d), after 2500s (e) and 5000s (f). (g). The electrochemical cycling performance of high loading NCM||Li metal pouch cell with different electrolytes. (h). The areal capacity-voltage curve of high loading NCM||Li metal pouch cell used E-1% $C_6F_3LiN_4$ as electrolyte during different cycles. (i). The photograph of LED light powered by the NCM||Li metal pouch cell.

deposition.

In order to further understand how the difference between the Li metal surfaces constructed by E-baseline and E-1% $C_6F_3LiN_4$ will affect the subsequent Li metal deposition, we use COMSOL software to simulate the entire Li metal deposition process. First, mark an area ($5\ \mu\text{m} \times 5\ \mu\text{m}$) in the SEM image after 10 cycles, and use this area as the initial state of Li metal deposition. Then the SEM image is converted into gray-scale image information, and the shades of the colors in the gray-scale image correspond to different heights. Therefore, it can be directly converted into a 3D height spectrum and used as COMSOL simulation model (Fig. S6). The uneven interface constructed by E-baseline results in uneven distribution of Li ions inside the SEI, and its concentration at the tip is very low, so it tends to attract more Li ions. When the same flow rate Li ions is transferred, the Li ions near the tip is higher than other places, thus aggravating the unevenness of Li metal deposition (Fig. 7a–c). By comparison, the Li metal interface constructed after 10 cycles of E-1% $C_6F_3LiN_4$ is smoother, so the Li ion flux in internal SEI is evenly distributed, interface formed after the deposition is continued to be smooth (Fig. 7d–f). Finally, in order to test the advantages of E-1% $C_6F_3LiN_4$ in actual battery applications, we used high-loading NCM cathode materials (loading of $16.12\ \text{mg}/\text{cm}^2$), and assembled pouch batteries (total capacity of 153 mAh) for testing, the test current is $2.9\ \text{mA}/\text{cm}^2$ (1C). Using a high-load NCM cathode material and E-1% $C_6F_3LiN_4$ as the electrolyte, the pouch battery can still have capacity retention rate of 81% after 25 cycles, while E-baseline is only 63% (Fig. 7g). And from the capacity-voltage curve of the initial 5 cycles of E-1% $C_6F_3LiN_4$, its overpotential has basically not changed, indicating that E-1% $C_6F_3LiN_4$ can still ensure the stability of its interface even in pouch battery with high current density, thus promoting improved cycle performance (Fig. 7h). The use of high loading NCM||Li pouch battery under E-1% $C_6F_3LiN_4$ electrolyte can light up the LED light, which also proves the feasibility of E-1% $C_6F_3LiN_4$ electrolyte in practical applications (Fig. 7i) [47,48].

4. Conclusion

In this work, $C_6F_3LiN_4$ was used as an additive to successfully build bi-electrode SEI film in Li metal-based battery. The characterization results show that $C_6F_3LiN_4$ built uniform protective film (7 nm) on NCM 523 particles to prevent the particles from being destroyed. The result of XPS spectra shows that E-1% $C_6F_3LiN_4$ can promote the increase of long chain organic components and inorganic components (LiF) in CEI. At the same time, the Li metal surface constructed by E-1% $C_6F_3LiN_4$ with more polycarbonate species can greatly reduce the fragmentation of SEI, and thus form a uniform deposition of Li metal in AFM images. As a result, the use high loading NCM||Li pouch battery under E-1% $C_6F_3LiN_4$ electrolyte exhibits $3.0\ \text{mAh}/\text{cm}^2$, and owns capacity retention rate of 81% after 25 cycles, while E-baseline is only 63%. Therefore, the $C_6F_3LiN_4$ additive can enable the long-time cycling of high loading NCM || Li metal-based batteries in practical application. Our work verifies the importance of simultaneously stabilizing the cathode and anode interfaces for the electrochemical performance of Li metal-based batteries.

CRedit authorship contribution statement

Zhipeng Wen: Conceptualization, Methodology, Supervision, Project administration, Writing – original draft. **Hang Li:** COMSOL simulation, Formal analysis, Validation, Writing – review & editing. **Huiyang Li:** Formal analysis, Visualization, Writing – review & editing. **Haiming Hua:** DFT simulation, Writing – review & editing. **Feng Wang:** Formal analysis, Visualization, Writing – review & editing. **Yu Gu:** Formal analysis, Visualization, Writing – review & editing. **Yang Yang:** Conceptualization, Data curation, Project administration, Writing – review & editing. **Jinbao Zhao:** Conceptualization, Supervision, Data curation, Project administration, Funding acquisition, Writing – review

& editing.

Declaration of competing interest

The authors declare that they have no known competing financial interests or personal relationships that could have appeared to influence the work reported in this paper.

Acknowledgments

This work was supported by the Fundamental Research Funds for the Central Universities (No. 20720190040) and National Natural Science Foundation of China (No. 21875198 and No. 21875195). The authors thank Pro. Peng Zhang, Dongzheng Wu at Xiamen University for their instructive discussions on manuscript revision and Sha Tan at CMB NETWORK TECHNOLOGY Co.,Ltd. for help in graphic editing.

Appendix A. Supplementary data

Supplementary data to this article can be found online at <https://doi.org/10.1016/j.jpowsour.2021.230370>.

References

- [1] Y. Yang, H. Zhu, J.F. Xiao, H.B. Geng, Y.F. Zhang, J.B. Zhao, G. Li, X.L. Wang, C. Li, Q. Liu, *Adv. Mater.* 32 (2020), e1905295.
- [2] Y. Yang, J.B. Zhao, *Adv. Sci.* (2021), 2004855.
- [3] P. Xu, X.Y. Hu, X.Y. Liu, X.D. Lin, X.L. Fan, X.Y. Cui, C. Sun, Q.H. Wu, X.B. Lian, R. M. Yuan, M.S. Zheng, Q.F. Dong, *Energy Storage Mater* 38 (2021) 190–199.
- [4] S.S. Chi, Y.C. Liu, W.L. Song, L.Z. Fan, Q. Zhang, *Adv. Funct. Mater.* 27 (2017), 1700348.
- [5] Y.T. He, Y.H. Zhang, P. Yu, F. Ding, X.F. Li, Z.H. Wang, Z. Lv, X.J. Wang, Z.G. Liu, X.Q. Huang, *J. Energy Chem.* 45 (2020) 1–6.
- [6] Z. Hou, J.L. Zhang, W.H. Wang, Q.W. Chen, B.H. Li, C.L. Li, *J. Energy Chem.* 45 (2020) 7–17.
- [7] H. Jiang, H.L. Fan, Z.X. Han, B. Hong, F.X. Wu, K. Zhang, Z.A. Zhang, J. Fang, Y. Q. Lai, *J. Energy Chem.* 54 (2021) 301–309.
- [8] H.J. Peng, J.Q. Huang, X.B. Cheng, Q. Zhang, *Adv. Energy Mater.* 7 (2017), 1700260.
- [9] W.J. Chen, C.X. Zhao, B.Q. Li, Q. Jin, X.Q. Zhang, T.Q. Yuan, X.T. Zhang, Z.H. Jin, S. Kaskel, Q. Zhang, *Energy Environ. Mater.* 3 (2020) 160–165.
- [10] X.D. Lin, Y. Gu, X.R. Shen, W.W. Wang, Y.H. Hong, Q.H. Wu, Z.Y. Zhou, D.Y. Wu, J. K. Chang, M.S. Zheng, B.W. Mao, Q.F. Dong, *Energy Environ. Sci.* 14 (2021) 1439–1448.
- [11] D.S. Hall, R. Gauthier, A. Eldesoky, V.S. Murray, J.R. Dahn, *ACS Appl. Mater. Interfaces* 11 (2019) 14095–14100.
- [12] H.Y. Li, A.R. Liu, N. Zhang, Y.Q. Wang, S. Yin, H.H. Wu, J.R. Dahn, *Chem. Mater.* 31 (2019) 7574–7583.
- [13] L.D. Lin, K. Qin, Q.H. Zhang, L. Gu, L.M. Suo, Y.S. Hu, H. Li, X.J. Huang, L.Q. Chen, *Angew. Chem., Int. Ed. Engl.* 60 (2021) 8289–8296.
- [14] L.W. Tan, Y. Sun, C.L. Wei, Y. Tao, Y. Tian, Y.L. An, Y.C. Zhang, S.L. Xiong, J. K. Feng, *Small* 17 (2021), e2007717.
- [15] G.W. Chen, Z.L. Gong, *J. Electrochem.* 27 (2021) 76–82.
- [16] D.M. Kang, K. Tang, J. Koh, W.B. Liang, J.P. Lemmon, *J. Energy Chem.* 44 (2020) 68–72.
- [17] Y.X. Lin, Z.P. Wen, J.X. Liu, D.Z. Wu, P. Zhang, J.B. Zhao, *J. Energy Chem.* 55 (2021) 129–135.
- [18] S.S. Zhang, *J. Power Sources* 162 (2006) 1379–1394.
- [19] Z.L. Liu, A.S. Yu, J.Y. Lee, *J. Power Sources* 81–82 (1999) 416–419.
- [20] X.Q. Zhang, X.B. Cheng, X. Chen, C. Yan, Q. Zhang, *Adv. Funct. Mater.* 27 (2017), 1605989.
- [21] E. Markevich, G. Salitra, D. Aurbach, *ACS Energy Lett* 2 (2017) 1337–1345.
- [22] S.S. Lin, J.B. Zhao, *ACS Appl. Mater. Interfaces* 12 (2020) 8316–8323.
- [23] M. Armand, P. Johansson, M. Bukowska, P. Szczeciński, L. Niedzicki, M. Marcinek, M. Dranka, J. Zachara, G. Żukowska, M. Marczewski, G. Schmidt, W. Wieczorek, *J. Electrochem. Soc.* 167 (2020), 070562.
- [24] D.W. McOwen, S.A. Delp, E. Paillard, C. Herriot, S.D. Han, P.D. Boyle, R. D. Sommer, W.A. Henderson, *J. Phys. Chem. C* 118 (2014) 7781–7787.
- [25] F. Lindgren, C. Xu, L. Niedzicki, M. Marcinek, T. Gustafsson, F. Björefors, K. Edstrom, R. Younesi, *ACS Appl. Mater. Interfaces* 8 (2016) 15758–15766.
- [26] N. Piao, X. Ji, H. Xu, X.L. Fan, L. Chen, S.F. Liu, M.N. Garaga, S.G. Greenbaum, L. Wang, C.S. Wang, X.M. He, *Adv. Energy Mater.* 10 (2020), 1903568.
- [27] J.M. Zheng, P.F. Yan, D.H. Mei, M.H. Engelhard, S.S. Cartmell, B.J. Polzin, C. M. Wang, J.G. Zhang, W. Xu, *Adv. Energy Mater.* 6 (2016), 1502151.
- [28] J. Betz, J.P. Brinkmann, R. Nolle, C. Lurenbaum, M. Kolek, M.C. Stan, M. Winter, T. Placke, *Adv. Energy Mater.* 9 (2019), 1900574.
- [29] X. Fan, L. Chen, O. Borodin, X. Ji, J. Chen, S. Hou, T. Deng, J. Zheng, C. Yang, S. C. Liou, K. Amine, K. Xu, C. Wang, *Nat. Nanotechnol.* 13 (2018) 715–722.

- [30] L.F. Zou, Z.Y. Liu, W.G. Zhao, H.P. Jia, J.M. Zheng, Y. Yang, G.F. Wang, J.G. Zhang, C.M. Wang, *Chem. Mater.* 30 (2018) 7016–7026.
- [31] X.M. Fan, G.R. Hu, B. Zhang, X. Ou, J.F. Zhang, W.G. Zhao, H.P. Jia, L.F. Zou, P. Li, Y. Yang, *Nano Energy* 70 (2020) 104450.
- [32] G.Q. Zhang, K. Lin, X.Y. Qin, L.H. Zhang, T. Li, F.Z. Lv, Y. Xia, W.J. Han, F.Y. Kang, B.H. Li, *ACS Appl. Mater. Interfaces* 12 (2020) 37034–37046.
- [33] Y.M. Liu, X.Y. Qin, S.Q. Zhang, Y.L. Huang, F.Y. Kang, G.H. Chen, B.H. Li, *Energy Storage Mater* 18 (2019) 320–327.
- [34] T. Li, X.Q. Zhang, P. Shi, Q. Zhang, *Joule* 3 (2019) 2647–2661.
- [35] Q. Wang, Z. Yao, C. Zhao, T. Verhallen, D.P. Tabor, M. Liu, F. Ooms, F. Kang, A. Aspuru-Guzik, Y.S. Hu, M. Wagemaker, B. Li, *Nat. Commun.* 11 (2020) 4188.
- [36] Q.F. Yang, M.N. Cui, J.L. Hu, F.L. Chu, Y.J. Zheng, J.J. Liu, C.L. Li, *ACS Nano* 14 (2020) 1866–1878.
- [37] H. Sun, G. Zhu, Y. Zhu, M.C. Lin, H. Chen, Y.Y. Li, W.H. Hung, B. Zhou, X. Wang, Y. Bai, M. Gu, C.L. Huang, H.C. Tai, X. Xu, M. Angell, J.J. Shyue, H. Dai, *Adv. Mater.* 32 (2020) 2001741.
- [38] T. Kubota, M. Ihara, S. Katayama, H. Nakai, J. Ichikawa, *J. Power Sources* 207 (2012) 141–149.
- [39] H. Nakai, T. Kubota, A. Kita, A. Kawashima, *J. Electrochem. Soc.* 158 (2011) A798.
- [40] C. Xu, G. Hernandez, S. Abbrent, L. Kober, R. Konefal, J. Brus, K. Edstrom, D. Brandell, J. Mindemark, *ACS Appl. Energy Mater.* 2 (2019) 4925–4935.
- [41] K.N. Wood, E. Kazyak, A.F. Chadwick, K.H. Chen, J.G. Zhang, K. Thornton, N. P. Dasgupta, *ACS Cent. Sci.* 2 (2016) 790–801.
- [42] K.N. Wood, M. Noked, N.P. Dasgupta, *ACS Energy Lett* 2 (2017) 664–672.
- [43] S.J. Zhang, Z.G. Gao, W.W. Wang, Y.Q. Lu, Y.P. Deng, J.H. You, J.T. Li, Y. Zhou, L. Huang, X.D. Zhou, S.G. Sun, *Small* 14 (2018), e1801054.
- [44] S.D. Xu, Q.C. Zhuang, J. Wang, Y.Q. Xu, Y.B. Zhu, *Int. J. Electrochem. Sci.* 8 (2013) 8058–8076.
- [45] E. Markevich, G. Salitra, F. Chesneau, M. Schmidt, D. Aurbach, *ACS Energy Lett* 2 (2017) 1321–1326.
- [46] V. Etacheri, O. Haik, Y. Goffer, G.A. Roberts, I.C. Stefan, R. Fasching, D. Aurbach, *Langmuir* 28 (2012) 965–976.
- [47] S.R. Chen, C.J. Niu, H. Lee, Q.Y. Li, L. Yu, W. Xu, J.G. Zhang, E.J. Dufek, M. S. Whittingham, S. Meng, J. Xiao, J. Liu, *Joule* 3 (2019) 1094–1105.
- [48] J. Cui, X. Chen, Z. Zhou, M. Zuo, Y. Xiao, N. Zhao, C. Shi, X. Guo, *Mater. Today Energy* 20 (2021) 100632.